Harnessing Enantioselective Optical Forces by Quasibound States in the Continuum

Renchao Jin,[1] Xianzhe Zhang,[2] Pengcheng Huo,[3,4] Ziqiang Cai,[2] Yanqing Lu,[3,4] Ting Xu,[3,4,*] and Yongmin Liu[1,2,†]
[1]Department of Mechanical and Industrial Engineering, Northeastern University, Boston, Massachusetts 02115, USA
[2]Department of Electrical and Computer Engineering, Northeastern University, Boston, Massachusetts 02115, USA
[3]National Laboratory of Solid-State Microstructures, Jiangsu Key Laboratory of Artificial Functional Materials, College of Engineering and Applied Sciences, Nanjing University, Nanjing 210093, China
[4]Collaborative Innovation Center of Advanced Microstructures, Nanjing 210093, China

(Received 30 December 2023; accepted 1 July 2024; published 19 August 2024)

Enantioselective optical forces have garnered significant attention, because they provide a noninvasive means to separate chiral objects. A promising approach to enhance enantioselective optical forces is spatially overlapping and boosting electric and magnetic fields to create giant superchiral fields. Here, we utilize metasurfaces composed of asymmetric silicon dimers that support two distinct quasibound states in the continuum (quasi BICs). By precisely engineering these quasi BICs, we achieve nearly perfect spatial overlap of electric and magnetic fields near their anticrossing point, resulting in a remarkable 10^4-fold enhancement of the superchiral field. Consequently, the enantioselective optical force exerting on a single molecule exhibits a substantial increase, with magnitude up to $\mathrm{pN/mW\,\mu m^2}$. Furthermore, by encircling the anticrossing point, we can switch the handedness of the superchiral field and the enantioselective optical force. Last, we analyze the dynamics of quasi-BIC-assisted chiral separation, highlighting its potential applications in chiral sensing and sorting, circular dichroism spectroscopy, and pharmacology.

DOI: 10.1103/PhysRevLett.133.086901

Introduction—Chirality, as one essential property of matter, widely exists in nature [1,2]. An object is chiral if it cannot be superimposed onto its mirror image. It is well known that many chemical and biological molecules are chiral. A pair of chiral molecules showing mirror symmetry with respect to each other is called enantiomers. Although enantiomers share the same chemical formula, they can have distinctly different functions in chemical and biological processes, resulting in positive or negative effects [3]. Therefore, the discrimination of enantiomers is of vital importance in the fields of chemistry, biology, and pharmaceutics.

Chiral separation, as the core of chiral discrimination, holds the potential to spatially or temporally screen enantiomers [4–21]. Recently, chiral optical forces have attracted wide interest [4–21], since they promise an all-optical method to improve the existing technologies, such as chiral column chromatography, for chiral separation. For example, chiral nanoparticles with opposite handedness can be pushed in opposite directions by lateral optical forces [5]. Nanometer-scale enantiomer separation using a subwavelength slot waveguide has been proposed [13]. These discoveries reveal the intriguing chiral light-matter interactions, which are essential to engineer chiral optical forces. In general, the chiral optical force has three contributions: the gradient forces originating from the electric and magnetic fields, respectively, and the optical force stemming from the superchiral field [5,11–13]. Notably, the first two contribute equally to the two enantiomers, while only the third contribution can impose opposite forces on the two enantiomers that can be potentially used for chiral separation. Therefore, enhancing the superchiral field is crucial for realizing effective chiral separation. The superchiral field can be quantitively characterized by the optical chirality density C [22–30]. Generally, a higher C indicates stronger chiral light-matter interactions. Various approaches have been proposed to enhance superchiral fields based on standing waves, plasmonic resonances, Mie resonances, etc. [13,21,26–30]. However, these methods still face limitations such as low quality factors (Q factors), weak field enhancement, and inadequate mode overlapping. Achieving high Q factors and perfect overlapping of electric and magnetic fields can facilitate the enhancement of superchiral fields.

Here, we propose utilizing quasibound states in the continuum (quasi BICs) to significantly enhance both the superchiral fields and the enantioselective optical force. BICs are modes that remain localized even though they exist in a continuous spectrum of radiating waves [31,32]. Theoretically they possess an infinite Q factor and incredible near-field enhancement, which can be used to boost the light-matter interaction processes [33–40]. However, it is not possible to observe BICs as their linewidth vanishes. Fortunately, by breaking the symmetry of the system, quasi

*Contact author: xuting@nju.edu.cn
†Contact author: y.liu@northeatern.edu

BICs with finite linewidth appear. In this work, we design a metasurface consisting of asymmetric dimers to excite two quasi BICs simultaneously with large Q factors. Interestingly, the two quasi BICs have similar distributions of the electric and magnetic fields. The anticrossing point of these two quasi BICs exhibits a significant increase in the Q factor and nearly perfect spatial overlap of the electric and magnetic fields within the dimer gap. Consequently, the superchiral field shows a remarkable 10^4-fold enhancement at the anticrossing point. As a result, we successfully achieve chiral separation of two molecules with opposite chirality. Furthermore, we demonstrate a nontrivial effect whereby the handedness of the superchiral fields changes the sign due to the rapid phase changes within the interband of the two quasi BICs. These findings provide new insights into the interplay of quasi BICs, superchiral fields, and chiral optical forces, which would lead to innovative techniques for enantioselective sensing, separation, and spectroscopy with high sensitivity and accuracy.

Results and discussion—Figures 1(a) and 1(b) schematically illustrate the unit cell of the designed metasurface, which consists of two silicon nanocubes positioned above a silica substrate. The surrounding medium is water. The initial length and width of the cubes are $L = 282.5$ nm and $W = 292.5$ nm, respectively, and the height is $H = 265$ nm. A narrow gap of $G = 41$ nm separates the two cubes, while the periodicity is $P = 700$ nm. We introduce a dissymmetry factor Δs to break the in-plane symmetry. The commercial electromagnetic solver COMSOL Multiphysics is employed for the full-wave simulations, with left-handed circularly polarized (LCP) light as the illumination. Figure 1(c) shows the simulated transmittance spectra, where three distinct dips correspond to three different resonant modes. Through multipole modes expansion, we can identify that these modes are toroidal dipole (TD), quasi BIC with toroidal dipole (quasi-BIC TD), and quasi BIC with electric quadrupole (quasi-BIC EQ) modes, respectively. Figure 1(d) shows the TD mode has the lowest Q factor and is insensitive to Δs. In contrast, the

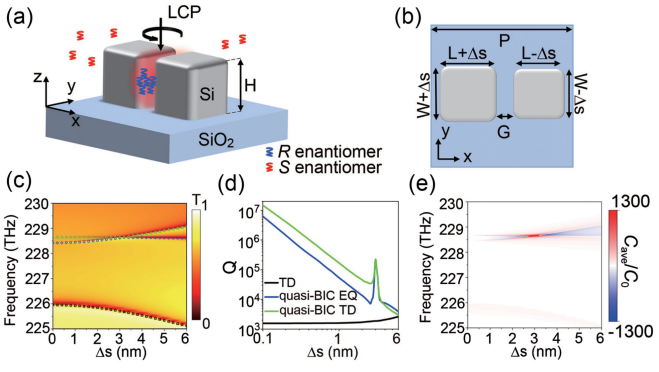

FIG. 1. (a),(b) Schematic of the unit cell of the metasurface. (c) Transmittance of the metasurface versus Δs. The black, blue, and green dotted lines represent the TD, quasi-BIC EQ, and quasi-BIC TD modes, respectively. (d) Corresponding Q factors. (e) Averaged optical chirality density within the gap of the cubes.

Q factors of the other two modes increase as Δs decreases [following a typical trend of $Q \propto (\Delta s/L)^{-2}$], and reach infinity when $\Delta s = 0$. Such features show the typical characteristics of geometric symmetry-protected BICs [38,40]. Consequently, after introducing symmetry breaking, these two modes convert to quasi BICs, where the dominated modes are quasi-BIC EQ and quasi-BIC TD, respectively. As illustrated in Figs. 1(c) and 1(d), we can observe the anticrossing of the two quasi BICs from the transmission spectra and simultaneously it causes a remarkable increase of Q factor. Intriguingly, the E field of quasi-BIC EQ and H field of quasi-BIC TD have similar spatial distribution inside the gap and their relative phase can be tuned to be around 90° when $\Delta s = 3$ nm (see Sec. S1 in Supplemental Material) [41]. These features, that is, a good spatial overlap of E and H fields with 90° phase difference, are expected to produce superchiral fields, thereby facilitating chiral separation [13,21,26–30]. Therefore, it is worthwhile to investigate the superchiral field within the gap at the anticrossing point.

The superchiral field can be quantitatively characterized by the optical chirality density C [19–29], which is defined as

$$C \equiv \frac{\varepsilon_0}{2} E \cdot \nabla \times E + \frac{1}{2\mu_0} B \cdot \nabla \times B = -\frac{\omega \varepsilon_0}{2} \mathrm{Im}(\boldsymbol{E}^* \cdot \boldsymbol{B}). \quad (1)$$

In Eq. (1), $E(\boldsymbol{E})$ and $B(\boldsymbol{B})$ represent the real (complex) the electric and magnetic field vectors, respectively. Physically, optical chirality density determines the degree of chiral asymmetry in the rate of excitation of a chiral molecule [22,23]. To compare the strength of optical chirality density, we can normalize it to the optical chirality density of circularly polarized light (CPL) in vacuum, i.e., $C_0 = \pm \omega \varepsilon_0 |E|^2/(2c)$, with $+$ $(-)$ corresponding to right (left) handedness of CPL. Figure 1(e) depicts the average chirality (C_{ave}) inside the gap of the cubes. The chirality map matches well with the trend of transmittance spectra in Fig. 1(c). Notably, the anticrossing point ($\Delta s = 3$ nm and $f = 228.66$ THz) manifests the highest average chirality, which holds 1300-fold enhancement. Counterintuitively, we observe the opposite signs of the C_{ave} inside the two quasi-BICs bands as shown in Fig. 1(e).

In Figs. 2(a)–2(c), we plot the C distributions in the y-z plane cut through the middle of the cubes gap for $\Delta s = 2.5$, 3, and 3.5 nm, respectively, while the frequency is fixed at 228.66 THz. They exhibit similar profiles but distinct handedness. To understand the opposite handedness of C, we compare electric and magnetic field distributions of the three cases. Although the field distributions are similar (see Fig. S3 in Supplemental Material) [41], the phase differences between the E_x and H_x components exhibit significant variations. Specifically, for $\Delta s = 3$ nm, the phase difference approaches 90°, while for $\Delta s = 2.5$ nm and 3.5 nm, it is approximately −110° due to the rapid phase change of the converged quasi BICs. Another noticeable result is the magnitude of the optical chirality

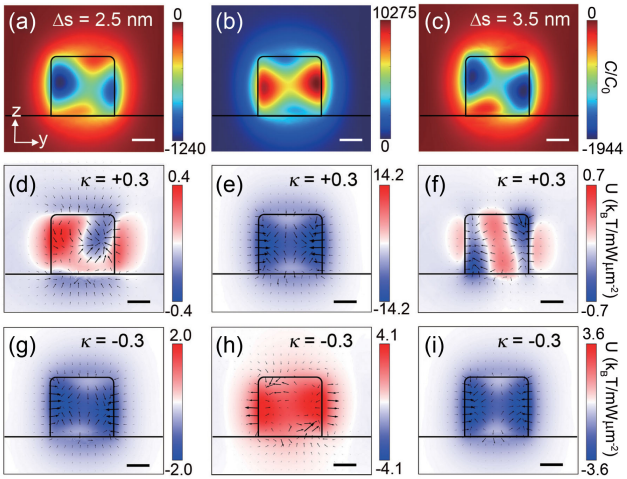

FIG. 2. (a)–(c) Normalized C distributions for $\Delta s = 2.5$, 3, and 3.5 nm, respectively. (d)–(f) Corresponding optical potential acting on a 10-nm-radius chiral nanoparticle with $\kappa = +0.3$, while (g)–(i) are the results for $\kappa = -0.3$. The black arrows indicate the direction and magnitude of the optical forces. All results are calculated under LCP incidence. Scale bar: 100 nm.

density. As shown in Fig. 2(b), the maximal enhancement of C reaches about 10 000. To the best of our knowledge, it is the highest value reported so far. Such an incredible enhancement of the superchiral field holds great potential for achieving effective chiral separation. Moreover, the requirement for Δs can be significantly alleviated by reducing the gap size while retaining the anticrossing effect (see Sec. S2 in Supplemental Material) [41].

In the following, we will quantify the chiral optical force induced by the quasi BICs of the metasurface, which is essential for chiral discrimination. The induced electric and magnetic dipole moments of a chiral nanoparticle can be modeled as [5]

$$\begin{bmatrix} \boldsymbol{p} \\ \boldsymbol{m} \end{bmatrix} = \begin{bmatrix} \alpha_{ee} & i\alpha_{em} \\ -i\alpha_{em} & \alpha_{mm} \end{bmatrix} \begin{bmatrix} \boldsymbol{E} \\ \boldsymbol{H} \end{bmatrix}. \tag{2}$$

Here, α_{ee}, α_{mm}, and α_{em} denote the complex electric, magnetic, and chiral polarizability of the nanoparticle, respectively. They are all related to the Pasteur parameter κ of the chiral nanoparticle, which describes the chiral response, as follows [2,5,11]:

$$\begin{aligned} \alpha_{ee} &= 4\varepsilon_0\pi r^3 \frac{(\varepsilon_r - \varepsilon_{rm})(\mu_r + 2) - \kappa^2}{(\varepsilon_r + 2\varepsilon_{rm})(\mu_r + 2) - \kappa^2}, \\ \alpha_{mm} &= -4\mu_0\pi r^3 \frac{\kappa^2}{(\varepsilon_r + 2\varepsilon_{rm})(\mu_r + 2) - \kappa^2}, \\ \alpha_{em} &= -12\pi r^3 \frac{j\kappa\sqrt{\varepsilon_0\mu_0}}{(\varepsilon_r + 2\varepsilon_{rm})(\mu_r + 2) - \kappa^2}. \end{aligned} \tag{3}$$

The radius of chiral nanoparticles in the simulations is set as $r = 10$ nm. The relative permittivity of the chiral nanoparticle and the surrounding material (water) are $\varepsilon_r = 2.1$ and $\varepsilon_{rm} = 1.77$, respectively, and the relative permeability is $\mu_r = 1$. As shown by Eq. (3), only the chiral polarizability α_{em} is proportional to Pasteur parameter κ, while α_{ee} and α_{mm} are independent of the sign of κ. The total optical force acting on such a chiral nanoparticle can be calculated by the following formula [5,11–13]:

$$\begin{aligned} \langle \boldsymbol{F} \rangle = &\frac{1}{4}\mathrm{Re}[\alpha_{ee}]\nabla|\boldsymbol{E}|^2 + \frac{1}{4}\mathrm{Re}[\alpha_{mm}]\nabla|\boldsymbol{H}|^2 \\ &+ \frac{1}{2}\mathrm{Im}[\alpha_{em}]\nabla\mathrm{Im}[\boldsymbol{E}\cdot\boldsymbol{H}^*]. \end{aligned} \tag{4}$$

The chiral optical potential can be obtained by integrating the force, which is given by

$$\langle U \rangle = \frac{1}{4}\mathrm{Re}[\alpha_{ee}]|\boldsymbol{E}|^2 + \frac{1}{4}\mathrm{Re}[\alpha_{mm}]|\boldsymbol{H}|^2 + \frac{1}{2}\mathrm{Im}[\alpha_{em}]\mathrm{Im}[\boldsymbol{E}\cdot\boldsymbol{H}^*]. \tag{5}$$

The first and second terms in Eq. (4) correspond to the gradient force originating from the electric field and magnetic field, respectively. They are independent of the handedness of the chiral nanoparticles. In constrast, the third term is related to the force resulting from the interaction between the chiral dipole (α_{em}) and the superchiral field. It is highly dependent on the handedness and Pasteur parameter κ of the chiral nanoparticle, and helps to separate chiral nanoparticles if optical chirality density C is sufficiently enhanced.

We have calculated the optical force and optical potential acting on an enantiomer pair, considering the three cases in Figs. 2(a)–2(c). The simulation results are presented in Figs. 2(d)–2(i). It is well known that a stable trapping requires a potential well with a depth of at least $10k_BT$, whereas weak trapping only needs to overcome the Brownian motion ($1k_BT$) [45]. From the calculated optical potential for a right-handed nanoparticle with $\kappa = +0.3$ [Figs. 2(d)–2(f)], it is clear that it can be stable trapped inside the gap when $\Delta s = 3$ nm [Fig. 2(e)], since the optical potential reaches $-14.2k_BT/\mathrm{mW}\,\mu\mathrm{m}^2$. However, in the cases of $\Delta s = 2.5$ nm [Fig. 2(d)] and $\Delta s = 3.5$ nm [Fig. 2(f)], the nanoparticle experiences a weak optical potential, indicates unsuccessful trapping of the nanoparticle. For a left-handed nanoparticle with $\kappa = -0.3$, the results are quite different as shown in Figs. 2(g)–2(i). For $\Delta s = 2.5$ nm [Fig. 2(g)] and $\Delta s = 3.5$ nm [Fig. 2(i)], the chiral nanoparticle can be attracted into the gap, but the magnitude of the optical potential only enables weak trapping. Interestingly, Fig. 2(h) demonstrates a pure positive optical potential inside the gap when $\Delta s = 3$ nm, indicating that the left-handed nanoparticle will be completely expelled from the gap. Therefore, the configuration of $\Delta s = 3$ nm can spatially separate enantiomers with

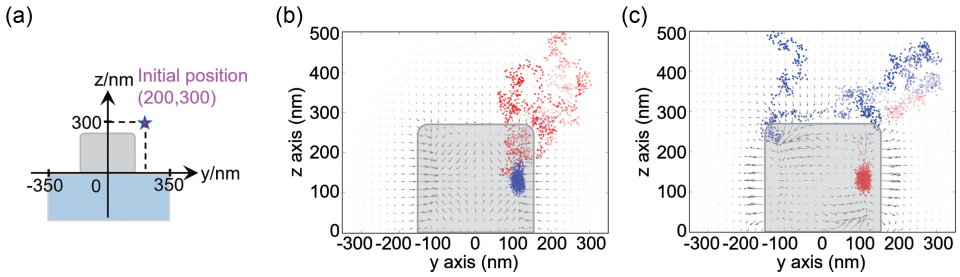

FIG. 3. (a) Illustration of the initial position of the enantiomers for the trajectory simulation. (b),(c) Trajectories of a right-handed particle with $\kappa = +0.3$ (blue), and left-handed particle with $\kappa = -0.3$ (red) nanoparticles under the illumination of (b) LCP and (c) RCP light, respectively. The power density used in the simulation is 1 mW μm^{-2}. The gray area represents the silicon nanocube. The simulation results are plotted in the yz plane cut through the middle of the gap.

$\kappa = \pm 0.3$, which is otherwise unachievable for the other two configurations.

We further investigate the chiral discrimination for $\Delta s = 3$ nm by calculating the trajectories of the two chiral nanoparticles within the gap. The trajectories of a particle in the presence of an external force can be calculated by the Langevin equation as follows [12,46,47]:

$$m\frac{d^2y(t)}{dt^2} = F_y(y,z) - \gamma\frac{dy(t)}{dt} + \sqrt{2k_BT\gamma}W(t),$$
$$m\frac{d^2z(t)}{dt^2} = F_z(y,z) - \gamma\frac{dz(t)}{dt} + \sqrt{2k_BT\gamma}W(t). \quad (6)$$

Here, m is the mass of the nanoparticle, and y and z represent the coordinates of the nanoparticle. F is the optical force acting on the chiral nanoparticle, and γ is the particle friction coefficient. $W(t)$ represents the white noise of Brownian motion with unit variance and zero mean. By applying the optical force in Fig. 2(b) to Eq. (6), we have calculated the nanoparticle trajectory over a period of 0.25 ms. The time step is 0.25 μs, and the initial coordinates of the nanoparticle are $(y, z) = (200\text{ nm}, 300\text{ nm})$ as illustrated in Fig. 3(a). In Figs. 3(b) and 3(c), the locations of $\kappa = +0.3$ and -0.3 chiral nanoparticles are plotted as blue and red dots, respectively. The incident light is LCP and right-handed circularly polarized (RCP) in Figs. 3(b) and 3(c), respectively. The optical forces for $\kappa = +0.3$ nanoparticle (black arrows) are plotted as a background for visual guidance. With LCP incidence, as shown by the blue dots in Fig. 3(b), the right-handed nanoparticle is trapped inside the gap and its locations match well with the optical potential profile in Fig. 2(e). On the contrary, the nanparticle with opposite handedness is expelled from the gap, as shown by the red dots in Fig. 3(b). The effects are reserved for RCP incidence as depicted in Fig. 3(c). Further discussions of chiral discrimination with different initial locations and gap sizes can be found in Sec. S3 of Supplemental Material [41]. Based on these results, it is evident that the configuration with $\Delta s = 3$ nm can successfully achieve chiral discrimination, while the other two configurations, with superchiral fields opposite in sign, fail to achieve chiral discrimination due to the insufficient enhancement of the superchiral field.

Finally, to investigate the working range of chiral separation by the metasurface when $\Delta s = 3$ nm, we calculate the chiral optical potential as κ is varied from -1 to $+1$, and the results are shown in Fig. 4. The chiral optical potential is extracted along a line across the center of the gap and parallel to the y axis. As shown in Fig. 4(a), the LCP illumination exhibits two opposite optical potential regions depending on the Pasteur parameter κ. The black dashed curve in Fig. 4(a) indicates the $U = 0\ k_BT$ boundary. For positive κ, the optical potential is always negative, which implies an attractive force acting on the chiral nanoparticle in the gap. Obviously, the magnitude of optical potential is large enough to overcome Brownian motion. While for negative κ, the positive optical potential (red region) indicates a repulsive force acting on the chiral

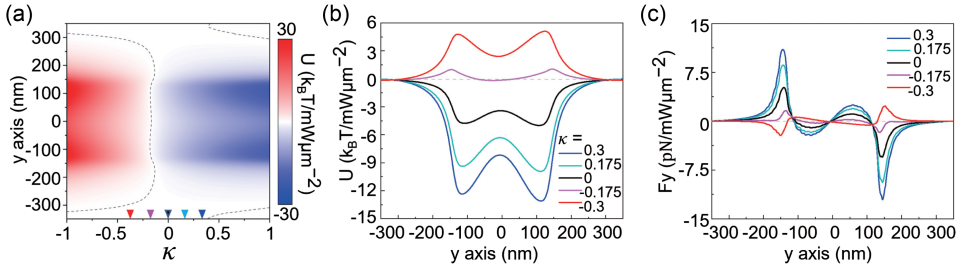

FIG. 4. (a) Optical potential on a chiral nanoparticle with different κ subject to LCP illumination. (b) Extracted optical potential and (c) optical force acting on the nanoparticle with chirality parameter $\kappa = -0.3$, -0.175, 0, 0.175, and 0.3, respectively.

nanoparticle. It is worth noting that the optical potential acting on the chiral nanoparticle with a small value of negative κ is still negative and shows an attractive trend. To make a better comparison, we select five chiral nanoparticles with different κ, as marked by triangles in Fig. 4(a), i.e., $\kappa = -0.3$, -0.175, 0, 0.175, and 0.3, respectively. The extracted optical potential is plotted in Fig. 4(b). As can be seen, both the blue curve (for $\kappa = 0.3$), cyan curve (for $\kappa = 0.175$), and black curve (for $\kappa = 0$) are below zero, indicating a trapping trend. The magenta curve (for $\kappa = -0.175$) crosses the zero, introducing uncertainty regarding whether the chiral nanoparticle is trapped or repelled in the gap. The red curve ($\kappa = -0.3$) is completely above zero, suggesting that the optical force is totally repulsive. To better understand these trends, the corresponding optical forces of these five cases are plotted in Fig. 4(c). In general, the attractive trend requires positive optical force at the $-y$ axis and meanwhile negative optical force at the $+y$ axis [blue, cyan, and black lines in Fig. 4(c)]. As for the magenta line, although it has a similar shape to that of the optical force, the magnitude is not sufficient to provide a trapping trend. The red line shows the opposite line shape, and the optical force has sufficient magnitude to repel nanoparticles in the gap.

Conclusions—In conclusion, we numerically demonstrate chiral separation using asymmetric silicon dimers that support quasi BICs. The anticrossing point of two quasi-BIC modes exhibits an unprecedented enhancement of superchiral fields, reaching a value of 10^4. Through the analysis of the chiral optical potential and the chiral optical force, we successfully identify the chiral discrimination on a pair of enantiomers with different handedness. The optical chirality density plays a crucial role in enhancing the interaction between chiral light and chiral nanoparticles, resulting in optical potential and optical force with magnitudes surpassing the state of the art. We envision that by further enhancing the fields through high Q-factor resonances, it will be possible to achieve chiral discrimination of molecules at the nanoscale. These findings open up new possibilities for all-optical chiral discrimination utilizing quasi BICs or other high-Q resonances. Such advancements have significant implications in the fields of chiral sensing and sorting, circular dichroism spectroscopy, and pharmacology.

Acknowledgments—Y. Liu acknowledges the financial support of the National Science Foundation (CBET-1931777 and DMR-2202268).

[1] J. Lough and I. W. Wainer, *Chirality in the Natural & Applied Sciences* (Blackwell Publishing Limited, Oxford, 2002).

[2] I. V. Lindell, A. H. Sihvola, S. A. Tretyakov, and A. J. Viitanen, *Electromagnetic Waves in Chiral and Bi-isotropic Media*, 1st ed. (Artech House, London, 1994).

[3] L. A. Nguyen, H. He, and C. Pham-Huy, Chiral drugs: An overview, Int. J. Biomed. Sci. **2**, 85 (2006).

[4] T. J. Ward and B. A. Baker, Chiral separations, Anal. Chem. **80**, 4363 (2008).

[5] S. B. Wang and C. T. Chan, Lateral optical force on chiral particles near a surface, Nat. Commun. **5**, 3307 (2014).

[6] T. Zhang, M. R. C. Mahdy, Y. Liu, J. H. Teng, C. T. Lim, Z. Wang, and C. W. Qiu, All-optical chirality-sensitive sorting via reversible lateral forces in interference fields, ACS Aano **11**, 4292 (2017).

[7] D. S. Bradshaw and D. L. Andrews, Chiral discrimination in optical trapping and manipulation, New J. Phys. **16**, 103021 (2014).

[8] G. Tkachenko and E. Brasselet, Optofluidic sorting of material chirality by chiral light, Nat. Commun. **5**, 3577 (2014).

[9] G. Tkachenko and E. Brasselet, Helicity-dependent three-dimensional optical trapping of chiral microparticles, Nat. Commun. **5**, 4491 (2014).

[10] Y. Shi, T. Zhu, T. Zhang, A. Mazzulla, D. P. Tsai, W. Ding, A. Q. Liu, G. Cipparrone, J. J. Sáenz, and C. W. Qiu, Chirality-assisted lateral momentum transfer for bidirectional enantioselective separation, Light Sci. Appl. **9**, 62 (2020).

[11] Y. Zhao, A. A. E. Saleh, and J. A. Dionne, Enantioselective optical trapping of chiral nanoparticles with plasmonic tweezers, ACS Photonics **3**, 304 (2016).

[12] T. Cao and Y. Qiu, Lateral sorting of chiral nanoparticles using Fano-enhanced chiral force in visible region, Nanoscale **10**, 566 (2018).

[13] L. Fang and J. Wang, Optical trapping separation of chiral nanoparticles by subwavelength slot waveguides, Phys. Rev. Lett. **127**, 233902 (2021).

[14] M. Liu, T. Zentgraf, Y. Liu, G. Bartal, and X. Zhang, Light-driven nanoscale plasmonic motors, Nat. Nanotechnol. **5**, 570 (2010).

[15] A. Hayat, J. P. B. Mueller, and F. Capasso, Lateral chirality-sorting optical forces, Proc. Natl. Acad. Sci. U.S.A. **112**, 13190 (2015).

[16] R. P. Cameron, S. M. Barnett, and A. M. Yao, Discriminatory optical force for chiral molecules, New J. Phys. **16**, 013020 (2014).

[17] M. L. Solomon, J. Hu, M. Lawrence, A. García-Etxarri, and J. A. Dionne, Enantiospecific optical enhancement of chiral sensing and separation with dielectric metasurfaces, ACS Photonics **6**, 43 (2018).

[18] E. Mohammadi, K. L. Tsakmakidis, A. N. Askarpour, P. Dehkhoda, A. Tavakoli, and H. Altug, Nanophotonic platforms for enhanced chiral sensing, ACS Photonics **5**, 2669 (2018).

[19] Y. Liu, Z. Wu, D. W. Armstrong, H. Wolosker, and Y. Zheng, Detection and analysis of chiral molecules as disease biomarkers, Nat. Rev. Chem. **7**, 355 (2023).

[20] K. Yao and Y. Zheng, Near-ultraviolet dielectric metasurfaces: from surface-enhanced circular dichroism spectroscopy to polarization-preserving mirrors, J. Phys. Chem. C **123**, 11814 (2019).

[21] C. Genet, Chiral light–chiral matter interactions: An optical force perspective, ACS Photonics **9**, 319 (2022).

[22] Y. Tang and A. E. Cohen, Optical chirality and its interaction with matter, Phys. Rev. Lett. **104**, 163901 (2010).
[23] Y. Tang and A. E. Cohen, Enhanced enantioselectivity in excitation of chiral molecules by superchiral light, Science **332**, 333 (2011).
[24] K. Yao and Y. Liu, Enhancing circular dichroism by chiral hotspots in silicon nanocube dimmers, Nanoscale **10**, 8779 (2018).
[25] V. K. Valev, J. J. Baumberg, C. Sibilia, and T. Verbiest, Chirality and chiroptical effects in plasmonic nanostructures: Fundamentals, recent progress, and outlook, Adv. Mater. **25**, 2517 (2013).
[26] J. García-Guirado, M. Svedendahl, J. Puigdollers, and R. Quidant, Enantiomer-selective molecular sensing using racemic nanoplasmonic arrays, Nano Lett. **18**, 6279 (2018).
[27] C. S. Ho, A. Garcia- Etxarri, Y. Zhao, and J. A. Dionne, Enhancing enantioselective absorption using dielectric nanospheres, ACS Photonics **4**, 197 (2017).
[28] J. Hu, M. Lawrence, and J. A. Dionne, High quality factor dielectric metasurfaces for ultraviolet circular dichroism spectroscopy, ACS Photonics **7**, 36 (2019).
[29] J. Garcia-Guirado, M. Svedendahl, J. Puigdollers, and R. Quidant, Enhanced chiral sensing with dielectric nanoresonators, Nano Lett. **20**, 585 (2019).
[30] Y. Chen, C. Zhao, Y. Zhang, and C. W. Qiu, Integrated molar chiral sensing based on high-Q metasurface, Nano Lett. **20**, 8696 (2020).
[31] C. W. Hsu, B. Zhen, A. D. Stone, J. D. Joannopoulos, and M. Soljačić, Bound states in the continuum, Nat. Rev. Mater. **1**, 1 (2016).
[32] M. V. Rybin, K. L. Koshelev, Z. F. Sadrieva, K. B. Samusev, A. A. Bogdanov, M. F. Limonov, and Y. S. Kivshar, High-Q supercavity modes in subwavelength dielectric resonators, Phys. Rev. Lett. **119**, 243901 (2017).
[33] A. Kodigala, T. Lepetit, Q. Gu, B. Bahari, Y. Fainman, and B. Kanté, Lasing action from photonic bound states in continuum, Nature (London) **541**, 196 (2017).
[34] K. Koshelev, S. Kruk, E. Melik-Gaykazyan, J. H. Choi, A. Bogdanov, H. G. Park, and Y. Kivshar, Subwavelength dielectric resonators for nonlinear nanophotonics, Science **367**, 288 (2020).
[35] S. T. Ha, Y. H. Fu, N. K. Emani, Z. Pan, R. M. Bakker, R. Paniagua-Domínguez, and A. I. Kuznetsov, Directional lasing in resonant semiconductor nanoantenna arrays, Nat. Nanotechnol. **13**, 1042 (2018).
[36] C. Huang, C. Zhang, S. Xiao, Y. Wang, Y. Fan, Y. Liu, N. Zhang, G. Qu, H. Ji, J. Han, L. Ge, Y. Kivshar, and Q. Song, Ultrafast control of vortex microlasers, Science **367**, 1018 (2020).
[37] J. Jin, X. Yin, L. Ni, M. Soljačić, B. Zhen, and C. Peng, Topologically enabled ultrahigh-Q guided resonances robust to out-of-plane scattering, Nature (London) **574**, 501 (2019).
[38] Z. Liu, Y. Xu, Y. Lin, J. Xiang, T. Feng, Q. Cao, J. Li, S. Lan, and J. Liu, High-Q quasibound states in the continuum for nonlinear metasurfaces, Phys. Rev. Lett. **123**, 253901 (2019).
[39] A. Leitis, A. Tittl, M. Liu, B. H. Lee, M. B. Gu, Y. S. Kivshar, and H. Altug, Angle-multiplexed all-dielectric metasurfaces for broadband molecular fingerprint retrieval, Sci. Adv. **5**, eaaw2871 (2019).
[40] K. Koshelev, S. Lepeshov, M. Liu, A. Bogdanov, and Y. Kivshar, Asymmetric metasurfaces with high-Q resonances governed by bound states in the continuum, Phys. Rev. Lett. **121**, 193903 (2018).
[41] See Supplemental Material at http://link.aps.org/supplemental/10.1103/PhysRevLett.133.086901, which includes Refs. [42–44], for additional information about the multipole mode analysis, the impact of gap size on the superchiral fields, and the trajectories of chiral nanoparticles at different locations.
[42] Z. G. Dong, J. Zhu, X. B. Yin, J. Q. Li, C. Q. Lu, and X. Zhang, All-optical Hall effect by the dynamic toroidal moment in a cavity-based metamaterial, Phys. Rev. B **87**, 245429 (2013).
[43] T. Kaelberer, V. A. Fedotov, N. Papasimakis, D. P. Tsai, and N. I. Zheludev, Toroidal dipolar response in a metamaterial, Science **330**, 1510 (2010).
[44] R. C. Jin, J. Li, Y. H. Wang, M. J. Zhu, J. Q. Li, and Z. G. Dong, Optical force enhancement and annular trapping by plasmonic toroidal resonance in a double-disk metastructure, Opt. Express **24**, 27563 (2016).
[45] A. Ashkin, J. M. Dziedzic, J. E. Bjorkholm, and S. Chu, Observation of a single-beam gradient force optical trap for dielectric particles, Opt. Lett. **11**, 288 (1986).
[46] P. Hansen, Y. Zheng, J. Ryan, and L. Hesselink, Nanooptical conveyor belt, part I: Theory, Nano Lett. **14**, 2965 (2014).
[47] P. H. Jones, O. M. Marago, and G. Volpe, *Optical Tweezers: Principles and Applications* (Cambridge University Press, Cambridge, England, 2015).